Distinguishing $d_{xz} + id_{yz}$ and $d_{x^2-y^2}$ pairing in Sr_2RuO_4 by high magnetic field H-T phase diagrams

R. Gupta [1,*] S. Shallcross,[2] J. Quintanilla,[3] M. Gradhand,[1,4] and J. Annett[1,†]

[1]*H. H. Wills Physics Laboratory, University of Bristol, Tyndall Avenue, Bristol BS8-1TL, United Kingdom*

[2]*Max-Born-Institute for Non-linear Optics, Max-Born Strasse 2A, 12489 Berlin, Germany*

[3]*Physics of Quantum Materials, School of Physical Sciences,University of Kent, Canterbury CT2 7NH, United Kingdom*

[4]*Institute of Physics, Johannes Gutenberg University Mainz, Staudingerweg 7, 55128 Mainz, Germany*

(Received 30 October 2021; revised 5 August 2022; accepted 29 August 2022; published 14 September 2022)

Employing a realistic tight-binding model describing the Fermi surface in the normal state of Sr_2RuO_4, we map out magnetic field versus temperature phase diagrams for $d_{x^2-y^2}(B_{1g})$ and $d_{xz} + id_{yz}(E_g)$ pairing types. Both produce (i) a similar Knight shift suppression of ∼80% and (ii) a bicritical point at $T = 0.88$ K separating low field second-order phase transitions from high-field Pauli limiting first-order transitions. We find, however, strikingly different phase behavior within the high-field Pauli limiting region. For $d_{x^2-y^2}$ pairing symmetry, an additional lower critical line of first-order transitions is found (terminating in a critical point at $T = 0.09$-0.22 K depending on the choice of Hubbard U parameters), while for $d_{xz} + id_{yz}$ no such additional high-field phase transitions are found for any choice of Hubbard U. In conjunction with our earlier finding [Phys. Rev. B **102**, 235203 (2020)] for p-wave helical pairing of a still different high-field phase structure (a lower critical field line meeting the upper critical field line exactly at the bicritical point), we suggest high-field Pauli limiting phase structure as a possible route to distinguish pairing symmetries in this material.

DOI: 10.1103/PhysRevB.106.115126

I. INTRODUCTION

For many years, the prevailing view of Sr_2RuO_4 was of a well-understood Fermi liquid state [1] with a phase transition to an unconventional p-wave triplet superconductor [2–7] of $p_x + ip_y$ order parameter at $T_c = 1.5$ K. Recent experiments, reporting significant suppression of the Knight shift below T_c [8–10], decisively exclude this scenario. The nature of the pairing symmetry in Sr_2RuO_4 is thus now the focus of renewed and intense research interest: the parity [8], number of components [11,12], and even whether the pairing breaks time-reversal symmetry (TRS) [6,7,13,14] are all the subject of intense discussion amidst conflicting experimental evidence. In such a situation, observables that can distinguish between different pairing types are of immense value, and the purpose of the present paper is to suggest a property that it appears has not, to date, been considered as a pathway to discriminate pairing types.

With p-wave pairing perhaps ruled out [9,15,16], as both chiral or helical pairing types appear not to be able to capture the very strong (∼80%) suppression of the Knight shift [17,18], attention has turned to even-parity d-wave pairing [11,12,19]. The most natural d-wave candidates are the TRS breaking chiral $d_{xz} + id_{yz}$ (E_g) and TRS preserving $d_{x^2-y^2}$ (B_{1g}) order parameters. Discontinuity of elastic constants at T_c [11,12] and zero-field muon spectroscopy together strongly imply a multicomponent order parameter breaking time-reversal symmetry, pointing towards E_g pairing. However, this would lead to discontinuities in both elastic constants c_{66} and $(c_{11} - c_{12})/2$, with only the former observed [11,12]. On the other hand, Bogoliubov quasiparticle interference [20] shows clear evidence of vertical line nodes at $k_x = \pm k_y$, and the E_g pairing type has horizontal line nodes in the plane $k_z = 0$, thus this experiment is inconsistent with E_g pairing. This latter finding in fact supports the B_{1g} pairing type, which has exactly such (symmetry-imposed) line nodes [21]. More exotic multicomponent order parameters ($s \pm id$, $d \pm ig$) [11,12] have been suggested to reconcile these conflicting experiments, but these only produce the observed single superconducting transition as an accidental degeneracy of coupling constants; any change in these, e.g., by compression of the lattice, would then be expected to lead to distinct superconducting transitions for each component, which has not been observed. Elucidating experimental pathways to distinguish pairing states in Sr_2RuO_4 thus becomes a key task for progress in understanding this fascinating material.

One of the most fundamental properties of any material is its phase diagram: the structure of the phase boundaries, the nature of the transitions across them, and how they connect via multicritical points. The temperature–magnetic-field phase diagram of Sr_2RuO_4 has a well-characterized bicritical point at $T = 0.8$ K and $H = 1.2$ T at which the low-field second-order transition goes over to a first-order Pauli limiting transition [17,22–27]. Employing a realistic three-dimensional tight-binding model that captures very well the normal-state electronic structure, we explore the H-T phase diagram for the two even-parity d-wave pairing types $d_{xz} + id_{yz}$ and $d_{x^2-y^2}$. We find for both pairing types (i) a similar Knight shift suppression of ∼80%, and (ii) a bicritical

*Present address: School of Physics and CRANN, Trinity College, Dublin 2, Ireland; GUPTARE@tcd.ie

†James.Annett@bristol.ac.uk

point of 0.88 K separating lines of first and second transitions. Strikingly, however, these pairing symmetries generate dramatically different phase boundary structures within the high-field Pauli limiting region: while $d_{x^2-y^2}$ shows an additional lower critical field line of first-order transitions ending in a critical point at $T = 0.09$-0.22 K depending on the choice of Hubbard U parameters, $d_{xz} + id_{yz}$ pairing shows no such additional phase boundary for any choice of Hubbard U.

In conjunction with our previous finding [17] of a different high-field phase diagram structure for helical pairing, the phase structure of the Pauli limiting regime would appear to represent a path to distinguish pairing symmetries in this material. While such upper and lower critical field phase lines have been observed in a number of previous experimental works [22,28,29], they have been found to be sensitive to disorder, with lower mean field path (i.e., lower quality) samples not showing the additional lower critical field seen in higher quality samples [28]. Recently a double-horn structure in the NMR spectrum, highly reminiscent of the high-field phase boundary lines seen in earlier experiments, has been reported [29]. In light of our findings, we suggest that experiments to establish conclusively the high-field phase diagram of this material could be used as a route to definitively rule out potential candidate pairing states.

II. TIGHT-BINDING MODEL

A realistic three-dimensional tight binding (TB) model [30] was previously used to study the p-wave chiral [31] and helical pairings [17] in Sr_2RuO_4. This tight-binding model, which describes the experimental Fermi surface very well, has been successfully deployed in many publications since its introduction by Annett *et al.* in 2003 [30]. Motivated by this, we employ here the same model to study the d-wave pairing state where the effective pairing Hamiltonian is a multiband attractive U Hubbard model with an "off-site" pairing

$$\hat{H} = \sum_{ijmm'\sigma} [(\varepsilon_m - \mu)\delta_{ij}\delta_{mm'} - t_{mm'}(ij)]c^{\dagger}_{im\sigma}c_{jm'\sigma} - \frac{1}{2}\sum_{ijmm'\sigma\sigma'} U^{\sigma\sigma'}_{mm'}(ij)\hat{n}_{im\sigma}\hat{n}_{jm'\sigma'} + \hat{H}_{\rm so};$$

$$\hat{H}_{\rm so} = -i\frac{\lambda}{2}\sum_{i,\sigma,\sigma'}\sum_{m,m'}\varepsilon^{\kappa mm'}\sigma^{\kappa}_{\sigma\sigma'}c^{\dagger}_{im\sigma}c_{im'\sigma'}, \quad (1)$$

where m and m' stand for the three ruthenium t_{2g} orbitals $a = d_{xy}$, $b = d_{xz}$, $c = d_{yz}$, and i, j refer to the sites of a body-centered-tetragonal lattice. We additionally include spin-orbit coupling (SOC), the last term, where $\sigma^{\kappa}_{\sigma\sigma'}$, $\kappa = x, y, z$ are the Pauli matrices, $\varepsilon^{\kappa mm'}$ denotes the completely antisymmetric tensor, and within our notation the Ru orbital indices ordered as $m = (a, b, c)$. λ represents the strength of the SOC, which following Robbins *et al.* has the value 12.5 meV [32].

This value of the SOC constant is considerably lower than the values recently reported in angle-resolved photoemission spectroscopy (ARPES) experiments [33], with supporting dynamical mean-field theory (DMFT) calculations deducing a large effective SOC of 200 meV (a result in keeping with early neutron scattering experiments [34]). As discussed by Robbins *et al.*, the value of 12.5 meV arises as the hopping parameters of our tight-binding model are fitted to the experimental band structure (Fermi surface areas, bandwidth, and cyclotron masses), while the value of SOC must necessarily be taken from the Γ point splitting found in density functional theory (DFT) *ab initio* calculations, which comes out to be 100 meV. However, in these DFT calculations the bandwidth is significantly larger (approximately four times larger) than experiment, and combining an *ab initio* derived SOC with an experimentally parametrized TB model requires rescaling to maintain a correct balance between bandwidth and spin-orbit-coupling induced Γ point splitting. A gap of 100 meV leads in our notation to a SOC parameter $\lambda = 50$ meV, which by the rescaling by the factor of 4 then yields $\lambda = 12.5$ meV, the value used in the model. This preserves the good agreement between our tight-binding derived Fermi surface and experiment, while using directly the SOC value from *ab initio* leads to a complete rearrangement of the Fermi surface and a marked disagreement with experiment.

The hopping integrals $t_{mm'}(ij)$ and on-site energies ε_m that have been reported in Ref. [30], and are reproduced in Table I, were fitted to reproduce the experimentally determined Fermi surface [35] that consists of three sheets: α and β dominated by d_{xz} and d_{yz} character orbitals, and a Γ-centered sheet (denoted γ) dominated by d_{xy} character. The off-site pairing interaction involves two interaction constants U_a and $U_{b/c}$, also presented in Table I.

A. Pairing function

As Sr_2RuO_4 has a high-symmetry body-centered-tetragonal crystal structure, there exist many symmetry-allowed choices of the pairing function, corresponding to different irreducible representations of the point group symmetry [21]. In this work, we consider two most probable d-wave pairings in Sr_2RuO_4: $d_{xz} + id_{yz}$ (E_g irreducible representation), which is the simplest d-wave state with TRS breaking, and $d_{x^2-y^2}$ (B_{1g} irreducible representation), which has no TRS breaking, but would be expected from some spin fluctuation pairing models [16].

For the B_{1g} model, the most natural even-parity basis functions are given by

$$\cos k_x, \ \cos k_y, \quad (2)$$

while for the E_g model, these are

$$\sin\frac{k_x}{2}\cos\frac{k_y}{2}\sin\frac{k_z c}{2}, \ \cos\frac{k_x}{2}\sin\frac{k_y}{2}\sin\frac{k_z c}{2}, \quad (3)$$

which are the simplest basis functions having the symmetry required node in the $k_z = 0$ plane [36]. In addition, for the B_{1g} model we consider only in-plane nearest-neighbor pairing for all three orbitals. In this model, the symmetry of the pairing function does not allow coupling between the adjacent planes, and therefore we consider a 2D pairing model. On the contrary, for E_g pairing, symmetry prohibits in-plane pairing, and we consider coupling only between the adjacent planes. In general, the Hubbard U can be written as a 3×3 matrix in

TABLE I. On-site energies, tight-binding hopping parameters, and Hubbard U constants employed for studying the E_g and B_{1g} pairing states of Sr_2RuO_4.

	ϵ_a	ϵ_b	t	t'	t_b^x	t_c^x	$t_b^\perp$	$t_{ab}^\perp$	t_{bc}	$t_{bc}^\perp$	U	U'
E_g	−131.82	−116.15	−81.62	−36.73	−109.37	−6.56	0.26	−1.05	−8.75	−1.05	25.36	50.44
B_{1g}											19.2	79.21

orbital space as

$$U_{m,m'} = \begin{pmatrix} U_a & 0 & 0 \\ 0 & U_{b/c} & U_{b/c} \\ 0 & U_{b/c} & U_{b/c} \end{pmatrix} \tag{4}$$

with the only difference for the two models being that the U-parameters represent in-plane pairing for the B_{1g} model, whereas they correspond to out-of-plane pairing for the E_g model.

Following the approach of Ref. [31] and using the basis functions (2) and (3), the gap function can be written for E_g pairing as

$$\Delta_{ij}(\mathbf{k}) = \left(\Delta_{ij}^{\uparrow\downarrow,x} \sin\frac{k_x}{2}\cos\frac{k_y}{2} + i\Delta_{ij}^{\downarrow\uparrow,y}\cos\frac{k_x}{2}\sin\frac{k_y}{2} \right) \times \sin\frac{k_z c}{2}, \tag{5}$$

and for B_{1g} pairing as

$$\Delta_{ij}(\mathbf{k}) = \left(\Delta_{ij}^{\uparrow\downarrow,x}\cos k_x - \Delta_{ij}^{\downarrow\uparrow,y}\cos k_y \right). \tag{6}$$

The coefficients involved are given by

$$\Delta_{ij}^{\sigma\sigma',x} = 4U\sum_n \int d^3k\, u_{i,n}^{\sigma}(\mathbf{k}) v_{j,n}^{\sigma'\star}(\mathbf{k}) \sin\frac{k_x}{2} \times \cos\frac{k_y}{2}\sin\frac{k_z c}{2}[1 - 2f(T, E_n)] \tag{7}$$

for the E_g model, and by

$$\Delta_{ij}^{\sigma\sigma',x} = U\sum_n \int d^3k\, u_{i,n}^{\sigma}(\mathbf{k}) v_{j,n}^{\sigma'\star}(\mathbf{k}) \cos k_x \times [1 - 2f(T, E_n)] \tag{8}$$

for the B_{1g} pairing. Similar relations hold for the y-components $\Delta_{ij}^{\sigma\sigma',y}$. In these expressions, $f(T, E_n)$ is the Fermi function at a temperature T and eigenvalue E_n corresponding to the nth band. $U = U_a$ for a-a pairing and $U = U_{b/c}$ otherwise. Also, we include interorbital coupling between b and c orbitals in our model, though it is extremely weak.

Using the above equations, we solve the Bogoliubov–de Gennes (BdG) equation

$$\begin{pmatrix} \hat{H}_{\mathbf{k}}(\mathbf{r}) & \hat{\Delta}_{\mathbf{k}}(\mathbf{r}) \\ \hat{\Delta}_{\mathbf{k}}^{\dagger}(\mathbf{r}) & -\hat{H}_{-\mathbf{k}}^{*}(\mathbf{r}) \end{pmatrix} \begin{pmatrix} u_{n\mathbf{k}}(\mathbf{r}) \\ v_{n\mathbf{k}}(\mathbf{r}) \end{pmatrix} = E_{n\mathbf{k}} \begin{pmatrix} u_{n\mathbf{k}}(\mathbf{r}) \\ v_{n\mathbf{k}}(\mathbf{r}) \end{pmatrix}, \tag{9}$$

employing a $480 \times 480 \times 48$ k-mesh. The only unknown constants are the interaction parameters U_a and $U_{b/c}$. These are chosen such that there is a single superconducting critical temperature of 1.5 K. Under this requirement, we find

$$U_a = 0.3107\,t, \quad U_{b/c} = 0.618\,t \tag{10}$$

for E_g pairing, and

$$U_a = 0.2352\,t, \quad U_{b/c} = 0.9705\,t \tag{11}$$

for B_{1g} pairing, with $t = 0.081\,62$ eV. It should be noted that the presence of SOC in our model couples the orbitals together. Therefore, it is a realistic model in which the system is more likely to have a common superconducting transition.

We would also briefly remark that due to spin-orbit coupling when we diagonalize the Bogoliubov–de Gennes Hamiltonian, the Bogoliubov quasiparticle wave functions, $u_{nk}(\mathbf{r})$ and $v_{nk}(\mathbf{r})$, contain admixtures of all spin components. Therefore, in an external field both singlet and triplet pairing correlations $\langle c_{m\sigma}(\mathbf{k}) c_{m\sigma'}(-\mathbf{k})\rangle$ may exist at any specific point $\mathbf{k}$ in the Brillouin zone. However, the even spatial parity of the solution ensures any triplet components induced by spin-orbit coupling cancel during the Brillouin zone integration, and there is no triplet component to the order parameter when averaged over the whole Brillouin zone. Furthermore, as the pairing model assumes that pairing interactions only exist in the singlet B_{1g} or E_g channels, the orbital-dependent gap function $\Delta_{ij}(\mathbf{k})$ in Eqs. (5) and (6) only includes spin-singlet pairing. In this sense, our model is a pure spin-singlet model.

Finally, within our TB model a spin-only magnetic field $\mathbf{H} = (H_x, H_y, H_z)$ can be added to Eq. (9) by replacing $\hat{H}_{\mathbf{k}}(\mathbf{r})$ with

$$\hat{H}_{\mathbf{k}}(\mathbf{r}) = H_{\mathbf{k}}(\mathbf{r})\hat{\sigma}_0 + \mu_B\mu_0\hat{\boldsymbol{\sigma}}\cdot H, \tag{12}$$

with μ_B the Bohr magneton and μ_0 the vacuum permeability (in what follows, we set $\mu_0 = 1$ for convenience).

III. ZERO-FIELD PROPERTIES

To show the validity of our model, we will first explore the zero and low external field properties of Sr_2RuO_4 for the two pairing symmetries we consider: the gap structure on the Fermi surface, density of states, and zero-field specific heat. For each case, we find that the interaction parameters chosen above lead to good agreement with experiment and, moreover, comparably good agreement for both $d_{x^2-y^2}$ and $d_{xz} + id_{yz}$ pairing.

A. Gap structure

In Fig. 1 we show the superconducting gap $\Delta(\mathbf{k})$ on the Fermi surface, which is obtained by solving the BdG equation [Eq. (9)]. As can be seen from the scale bars,

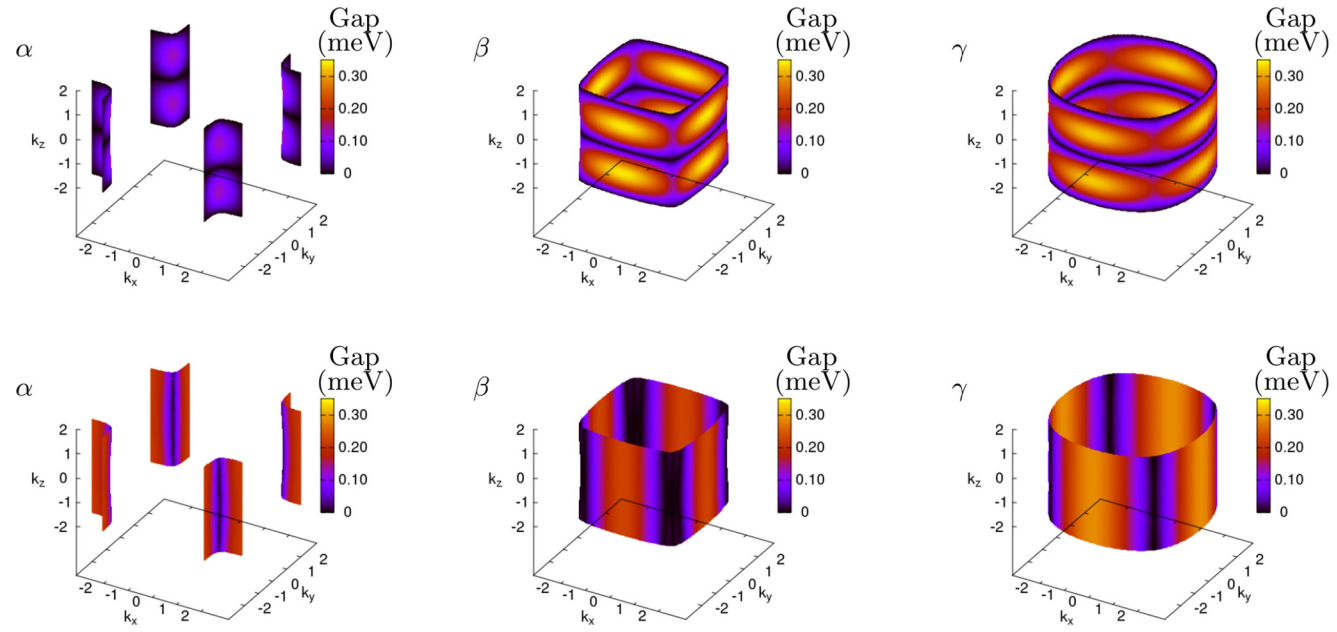

FIG. 1. Variation of zero-temperature superconducting gap on the three Fermi sheets of the normal state of Sr_2RuO_4. The top (bottom) row is for the E_g (B_{1g}) pairing. Whereas the E_g pairing has horizontal line nodes at $k_z = 0, \pm 2\pi/c$, B_{1g} has vertical line nodes at $k_x = \pm k_y$. k_x, k_y, and k_z are in units of the in-plane lattice constant $a = 3.862$ Å. $c = 12.722$ Å is the lattice constant along the z-axis.

the gap varies between 0 and ∼0.35 meV. Interestingly, ∼ 0.35 meV is also the maximum value of the single-particle superconducting gap reported in the Bogoliubov quasiparticle interference (BQPI) measurements [20] and also from differential conductance spectra [37,38]. The presence of nodes in the gap function can clearly be observed: as expected, these are horizontal for $d_{xz} + id_{yz}$ pairing and vertical for $d_{x^2-y^2}$ pairing, and they are found on each of the α, β, and γ Fermi sheets. The positions of these nodal lines can be readily understood from the gap functions in Eqs. (5) and (6): for $d_{xz} + id_{yz}$ pairing we have $\sin(k_z c/2) = 0$, yielding horizontal nodal lines at $k_z = 0$ and $k_z = \pm 2\pi/c$, while for $d_{x^2-y^2}$ pairing the corresponding condition is $\cos k_x = \cos k_y$, yielding vertical nodes when $k_x = \pm k_y$. These nodes contrast with the chiral and helical p-wave [17] scenarios, which have horizontal line nodes (though not symmetry-imposed) on the α and β sheets for $k_z = \pm\pi/c$ planes while the γ sheet has deep minima. Experiments on determining the nodal structure of the gap function have conflicting results: vertical line nodes are supported by thermal conductivity measurements and BQPI measurements [20], with horizontal line nodes by spin resonance in inelastic neutron scattering measurements [36] and specific-heat capacity measurements [39].

B. Density of states

In Fig. 2, we show the orbital-resolved and total superconducting density of states (DOS) for the two pairing functions. As expected, due to the presence of line nodes, the DOS is linear close to zero energy. The contribution to the total DOS from d_{xy}, d_{yz}, and d_{xz} orbitals is ∼58%, 21%, and 21%, respectively, in the normal state. The ratio for the orbital contribution $d_{yz} + d_{xz} : d_{xy} = 42 : 58$ matches well with the ratio of 43 : 57 for the contribution from $\alpha + \beta$ and γ bands from de Haas–van Alphen measurements [40]. The value of the superconducting gap 2Δ (the separation between the peaks in Fig. 2) is ∼0.56 meV, closely agreeing with tunneling spectroscopy measurements [37,38].

C. Specific heat

Correctly capturing the zero-field specific heat represents an important test of any theory of Sr_2RuO_4 as it is extremely sensitive to superconducting transitions. In Fig. 3 we show the orbital-resolved and total specific heat for the two pairing types we consider. As can be seen, a good agreement with the experimental specific heat [23] exists for both E_g pairing and B_{1g}, including for the magnitude of the superconducting jump. Note that the low-energy linear behavior with temperature is due to the presence of line nodes on the Fermi surface. The ratio of the contribution from d_{xy}, $d_{yz} + d_{xz}$ orbitals for the E_g and B_{1g} models near T_c is approximately 64 : 36 and 82 : 18, respectively.

IV. PROPERTIES AT FINITE FIELD

The physics of Sr_2RuO_4 in a magnetic field offers key insights into the pairing symmetry of the superconducting order parameter, notably the Knight shift for a-b plane oriented magnetic fields for which (in the absence of Fermi liquid corrections and SOC) theory predicts at $T = 0$ a 50% decrease in its value for helical p-wave pairing, no decrease for chiral p-wave pairing, and a 100% drop for d-wave pairing [21,41] under the application of a weak in-plane magnetic field. Here, we will first explore the spin polarization (in the normal and superconducting state), spin susceptibility, and specific heat, before constructing from the latter property the H-T phase diagram of $d_{xz} + id_{yz}$ and $d_{x^2-y^2}$ pairing in Sr_2RuO_4.

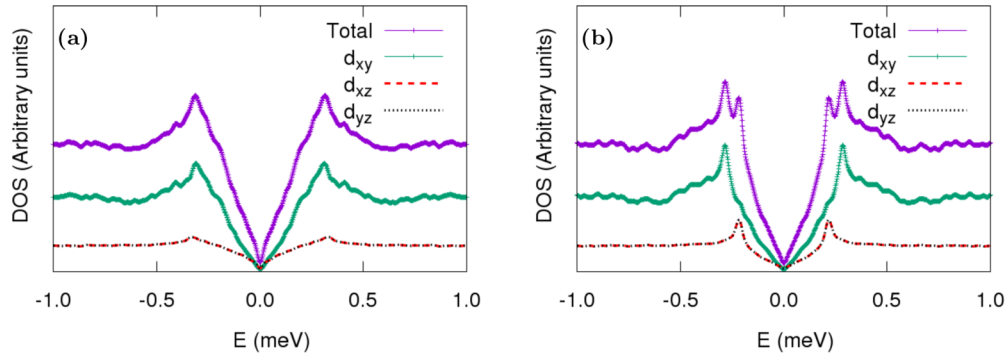

FIG. 2. Orbital-resolved and total superconducting density of states (DOS) for the (a) E_g and (b) B_{1g} model. Linear DOS at low energies is a consequence of the presence of nodal lines. Normal-state contribution to the total DOS from d_{xy}, d_{yz}, and d_{xz} orbitals is ∼58%, 21%, and 21%, respectively. The superconducting gap 2Δ from the separation between the peaks is ∼0.56 meV. At low energies, E_g pairing has a larger total DOS as compared to the B_{1g} pairing. Contribution from d_{xy} orbital dominates at nearly all energies in both models.

One should note that our magnetic field couples only with the spin degree of freedom, see Eq. (12) (although the presence of SOC can induce a small orbital magnetization), and so the vortex lattice contribution to the physics has been ignored. This is justifiable on the grounds that our primary interest is in Zeeman coupling of the field, as in experiment it is found that the material shows Pauli limiting under the application of an in-plane magnetic field. We will show from our calculations that this is indeed the case and thereby most of the physical properties considered here are dominated by spin rather than the vortex physics. However, the absence of vortex physics necessarily implies that a qualitative rather than quantitative agreement with critical magnetic fields and values of magnetic moments of experiments is to expected; as our focus is on elucidating qualitative physical properties of the E_g and B_{1g} pairing symmetries, this does not impede the message of our paper.

A. Spin moments and spin susceptibility

1. Spin moments

In Fig. 4 we present the ratio of the spin polarization in the superconducting and normal state (M_s/M_{normal}) as a function of temperature with the magnetic field held fixed. We set the field to ∼0.7 T in order to compare with the experimental data available from NMR measurements [10]. Also displayed in this figure are the 0.5 T data from PNS measurements [42]. The zero-temperature magnetization has a drop of ∼80% for both of the d-wave pairing models; turning off spin-orbit coupling in the calculation reduces this further to ∼90%. The ratio of M_s/M_{normal} is very close for both pairing types; for the E_g pairing, which breaks TRS, we also find a small orbital component [43]. The absence of the flux lattice contribution in particular means that quantitative agreement with PNS data at 0.06 K is not expected, as magnetic neutron diffraction couples to the total magnetic response (spin, orbital, and diamagnetic) with each component weighted equally. However, since the Knight shift is almost proportional to the spin polarization of the electrons, and the magnetic fields from orbital motion of electrons produce only a small shift, we expect a better agreement of our calculations with NMR results.

2. Spin susceptibility

In Fig. 5 we show the spin susceptibility ratio between the superconducting and the normal states as a function of field for $T = 25$ mK with the applied magnetic field scaled by the upper critical field. Also shown is the experimental data for the Knight shift obtained by NMR at two different oxygen positions [for O(1) at 66 mK [10] and for O(2) at 25 mK [8]], along with neutron scattering data measured at 60 mK [42] and 25 mK [44]. Within the broad scatter of experimental

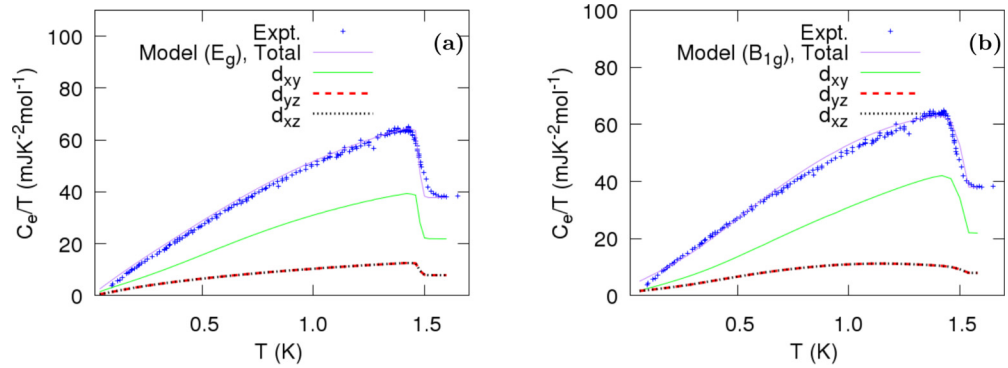

FIG. 3. Temperature variation of zero-field specific heat for (a) E_g and (b) B_{1g} pairing. Comparison with the experimental data [23] shows good agreement for both models. Linear behavior at low temperatures is due to the presence of line nodes. Overall, we see a somewhat better agreement for E_g pairing compared to the B_{1g} pairing.

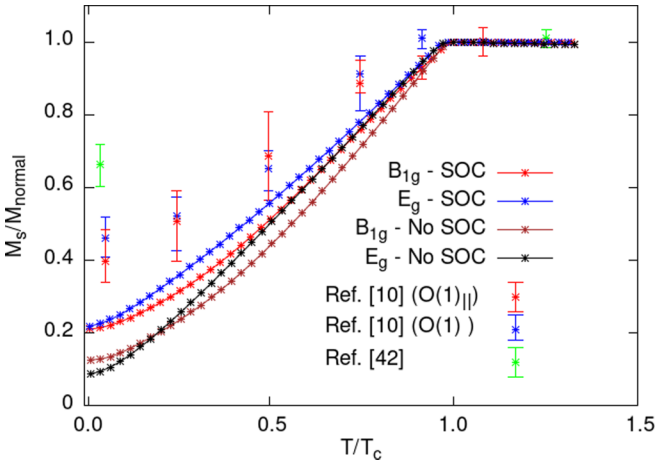

FIG. 4. Temperature variation of the ratio of spin moment in the superconducting and normal state at ∼0.7 T for $d_{xz} + id_{yz}$ (E_g) and $d_{x^2-y^2}$ (B_{1g}) pairing. Shown also are the same data with spin-orbit coupling (SOC) switched off. Experimental data for the Knight shift at 0.7 T from NMR measurements and PNS data at 0.5 T are also shown for comparison.

points, it can be seen that both pairing types agree well with the data. We note that the susceptibility ratio at zero field is evidently sensitive to the specific value of SOC coupling, and, as discussed in Sec. II, to maintain a balance of SOC splitting at the Γ point with the experimental bandwidth employed in our tight-binding model, our SOC is low compared to that retrieved from the latest experimental investigations [33]. We have checked that for larger values of SOC, while the offset at zero field does increase, it does not dramatically diminish

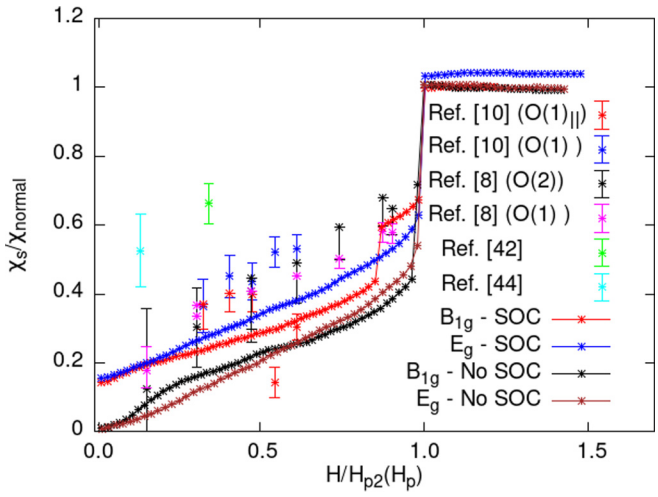

FIG. 5. Spin susceptibility ratio as a function of field for a temperature value of 25 mK for $d_{xz} + id_{yz}$ (E_g) and $d_{x^2-y^2}$ (B_{1g}) pairing. Also presented is experimental data for the Knight shift measured at two different positions of oxygen atoms at 66 mK [10] and at 25 mK [8] and the PNS data at 60 mK [42] and at 25 mK [44]. Note that the applied magnetic field has been divided by the critical field value H_p, which for the case of $d_{x^2-y^2}$ is chosen to be the upper critical field H_{p2}, see the discussion of the H-T phase diagram in Sec. IV C.

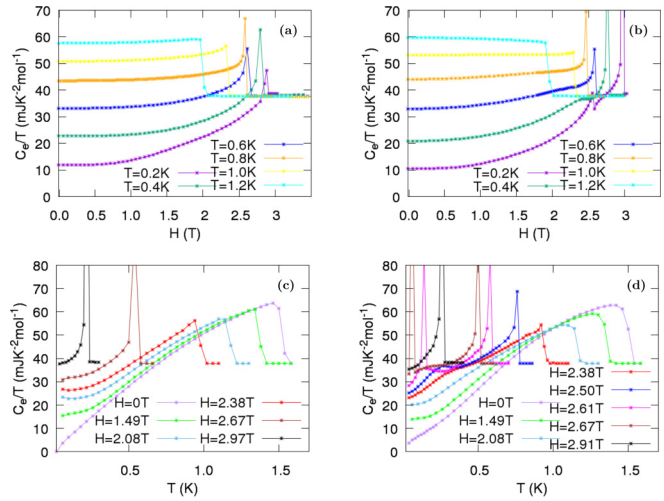

FIG. 6. Magnetic field variation of the specific heat for (a) $d_{xz} + id_{yz}$ pairing (E_g) and (b) $d_{x^2-y^2}$ pairing (B_{1g}) for a series of fixed temperatures. For temperatures less than $T \leqslant T^* = 0.88$ K, a clear change can be seen from a steplike feature to a pronounced peak, marking the onset of Pauli limiting at which the transition goes from second order to first order. Interestingly, the Pauli limiting onset temperature is identical for both pairing types, and it agrees well with the experimental value (0.8 K). While the heat capacity curves are very similar for both pairing types for the $T = 0.2$ K plot, a clear second peak can be seen for $d_{x^2-y^2}$ indicating a second superconducting transition, which does not occur for $d_{xz} + id_{yz}$ pairing. Similar behavior is seen in panels (c) and (d), in which is displayed the temperature variation with fixed field. In this case, the crossover field to Pauli limiting at $H^* \sim 2.38$ T is overestimated as compared to experiment (which finds $H^* \sim 1.2$ T), a result of coupling the spin-only coupling external field employed in the present work.

the agreement with the (rather broadly scattered) experimental data.

The magnitude of the Knight shift suppression, therefore, does not represent a quantity capable of discriminating between these d-wave pairing types. However, a striking difference can be seen: the susceptibility ratio for $d_{x^2-y^2}$ shows an addition jump after the critical field at which the superconducting transition occurs, indicating a second phase transition. Evidently, the large error bars preclude identification of this feature from the experimental data, and so we now turn to other signatures of this additional transition.

B. Specific heat

Presented in Figs. 6(a) and 6(b) is the specific heat for varying in-plane magnetic field for a series of fixed temperatures between $T = 0.2$ and 1.2 K. For both $d_{xz} + id_{yz}$ and $d_{x^2-y^2}$ pairing we see the evolution of pronounced peaks at the critical field at low temperatures to a steplike feature at higher temperatures, indicating a crossover from first-order to second-order transitions at the critical field. This crossover is due to Pauli limiting, and it has been observed in several experiments [22–27]. Interestingly, the temperature separating first- and second-order transitions is found to be the same for both pairing types. Reassuringly, while we fit our model parameters to reproduce the zero-field critical temperature, the

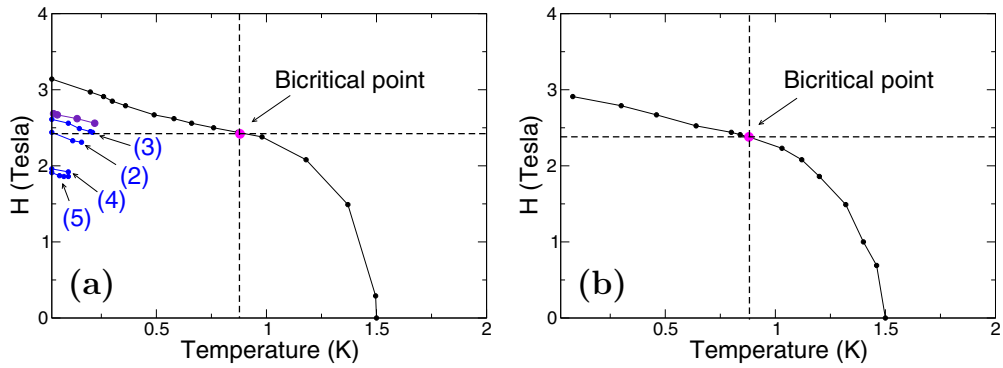

FIG. 7. H-T phase diagram for (a) $d_{x^2-y^2}$ pairing (B_{1g}) and (b) $d_{xz} + id_{yz}$ (E_g). For both pairing types, a bicritical point exists marking the onset of Pauli limited first-order transitions; we find $T^* = 0.88$ K and $H^* = 2.38$ T, the former in excellent quantitative with experiment, the latter overestimated due to the absence of the vortex lattice in our calculations. Strikingly, in the high-field low-temperature Pauli limiting regime, $d_{x^2-y^2}$ pairing shows an additional line of first-order transitions ending in a critical point at $T = 0.22$ K. The additional phase lines labeled (2–5) represent the variation of this additional phase line upon variation of the Hubbard U parameters of our model, for no choice of Hubbard U are additional phase structures seen for $d_{xz} + id_{yz}$ pairing. (Note that the variation of Hubbard U does not change the upper critical line or bicritical point significantly.)

value we find of $T^* = 0.88$ K agrees very closely with the experimental value of $T^* = 0.80$ K for the temperature onset of Pauli limiting.

While T^* is identical for both pairing types, the behavior within the Pauli limiting low-temperature and high-field regime is strikingly different. As can be noted from an examination of Fig. 6(b) for $T > T_{c2} = 0.2$ K, the specific-heat curves are nearly identical, while for $T \leqslant T_{c2}$ they become quite different. We see first a distinct shoulder in the specific heat at $T = 0.4$ K indicating the onset of a phase instability, which has evidently occurred by $T = 0.2$ K, where an additional peak in the heat capacity can clearly be seen.

Turning to the heat capacity for varying temperature with the in-plane magnetic field held fixed between $T = 0.2$ and 1.2 K in Figs. 6(c) and 6(d), we see (as expected) a similar behavior. While the heat capacities are very similar for field strengths of up to $H = 2.38$ T, for higher fields the $d_{x^2-y^2}$ pairing shows again the development of a shoulder feature (for $H = 2.38$ T) going over to a second peak that is clear in the curves for $H = 2.61$ and 2.67 T. For higher field strengths, a single transition is again seen. The field strengths for the onset of Pauli limiting behavior and the appearance of a second phase transition appear to be nearly identical. As expected, since we couple the field only to spin, the critical field for the onset of Pauli limiting first-order transitions is too high as compared to the field found in experiment (∼1.2 T) [28].

C. H-T phase diagrams

Finally, from these and data from other temperature and field slices, we construct the H-T phase diagrams of these two pairing types. These are shown in Fig. 7. As can be seen, the bicritical point (T^*, H^*) separating the Pauli limiting first order from the low-field second-order transitions is very similar for both pairing types ($T^* = 0.88$, $H^* = 2.42$) for B_{1g} and ($T^* = 0.88$, $H^* = 2.38$) for E_g; in a previous work, we found the same values of ($T^* = 0.8$, $H^* = 2.5$) for p-wave helical pairing [17] indicating that this feature is very robust to the superconducting order parameter. As noted above, while T^* agrees very well with experiment, the absence of a flux lattice in our calculations results in a much higher field value of the bicritical point than the 1.2 T [28] found in experiment. The additional transitions found for $d_{x^2-y^2}$ pairing can now clearly be seen as a line of additional first-order transitions below the upper critical field, terminating in a critical point [at $T = 0.22$ K and $H = 2.56$ T on line (3) in Fig. 7(a) for our choice of Hubbard parameters]. This additional phase behavior in the Pauli limiting regime represents a striking thermodynamic difference between the two pairing types. Therefore, whereas there is only one critical field (H_p) for the E_g pairing, two critical fields (H_{p1} and H_{p2}) exist for the B_{1g} pairing (with H_{p2} being only in a certain temperature interval).

The appearance of additional phase transitions in the Pauli limiting regime has been observed in, to the best of our knowledge, three previous experiments. In magnetic torque measurements, a lower critical line of first-order transitions was found in long mean field path samples, but not in (the presumably more disordered) samples of lower mean free path [28]. As we find here, this additional line of transitions extends from $T = 0$ with negative slope and terminates before the bicritical point. A double superconducting transition was observed in the heat capacity both for fixed field and fixed temperature [22], again indicating a negative slope of the additional line of transitions. Most recently, a "double-horn" feature in the NMR spectrum [29] has been reported (which, however, is attributed in that work to the presence of an FFLO state).

We should note that sensible variation of the Hubbard U parameters of our model does not qualitatively change these findings. In Fig. 7 we show the phase boundary lines obtained by four choices of Hubbard U parameters labeled (2)–(5), which are, in order, (0.2360,0.9500), (0.2300,0.9705), (0.2340,0.9200), and (0.2360,0.9100), with the number pair denoting the U_a and $U_{b/c}$ Hubbard U parameters, respectively (see Sec. II A) in units of $t = 0.081\,62$ eV. Each pair of Hubbard U parameters, which differ only by a few percent from those given in Sec. II A and used throughout this work, reproduce the zero field T_c of 1.5 K as well as the Knight shift

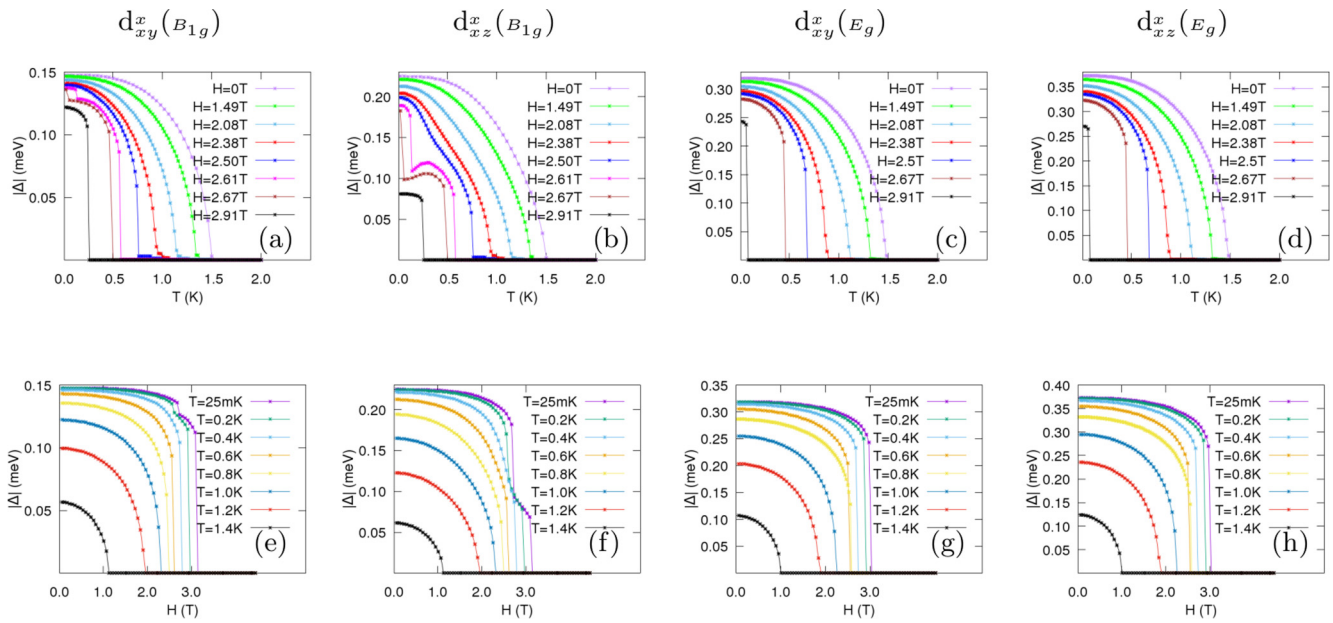

FIG. 8. Temperature variation of the x-component of the gap function on d_{xy} and d_{xz} orbitals for $d_{x^2-y^2}$ pairing (B_{1g}), panels (a) and (b), and $d_{xz}+id_{yz}$ pairing (E_g), panels (c) and (d). Clearly visible are the crossovers from second-order to first-order transitions with the onset of Pauli limiting, and the second additional transition for $d_{x^2-y^2}$ pairing in which a collapse of the gap function by nearly 50% of its value occurs on the α and β Fermi sheets (a small corresponding jump can be seen in d^x_{xy}, i.e., on the γ Fermi sheet, induced by spin-orbit coupling). Similar behavior can be seen for field variation at a fixed temperature, see panels (e) and (f), d_{xy} and d_{xz} orbitals for $d_{x^2-y^2}$ pairing, and (g) and (h), d_{xy} and d_{xz} orbitals for $d_{xz}+id_{yz}$ pairing.

suppression. However, as can be noted from Fig. 7, these different choices of Hubbard U parameters result in a variation of the critical end point in the range 0.09–0.22 K and a variation in the critical field over nearly 1 T. On the other hand, for all choices of Hubbard U parameters, the $d_{xz}+id_{yz}$ pairing never shows the additional phase line. We thus conclude that the finding of an additional phase transition in the Pauli limiting region for $d_{x^2-y^2}$ pairing but not $d_{xz}+id_{yz}$ pairing is robust within our model.

D. Gap function

In Fig. 8 we present the gap function for both fixed field varying temperature and vice versa. We first consider $d_{x^2-y^2}$ pairing, and panels (a), (b) present the x-component of Δ_{xy} and Δ_{xz}, respectively. Note that $\Delta^x_{xy}=\Delta^y_{xy}$ and $\Delta^x_{xz}=\Delta^y_{yz}$ due to the symmetry relations that to a numerically good approximation hold even in the presence of spin-orbit coupling. From these results, we see (i) the expected crossover from second order to first order at the onset of Pauli limiting, and (ii) that the additional line of phase transitions is driven by a partial collapse of the superconducting gap on the α and β Fermi sheets, with only a small feature present in Δ_{xy} arising due to the coupling induced by spin-orbit interaction. One can also note changes in curvature of the gap function before the onset of the additional first-order transition, and the curious feature of a very small increase in the superconducting gap as temperature is increased through the lower critical line. For $d_{xz}+id_{yz}$, pairing the gap function is somewhat larger and shows the expected crossover to Pauli limiting, but otherwise shows no distinguishing features. Fixing the temperature and varying field produces a very similar picture; for completeness, we show this data in panels (e), (f) of Fig. 8.

E. Origin of the difference of high-field behavior for B_{1g} and E_g pairing

We now examine the question of the origin of the difference in high-field behavior between the B_{1g} and E_g pairing symmetries, and we relate this to the orbital structure of the pairing interaction in each case.

The B_{1g} state involves mainly in-plane pairing, and it can therefore exist on the γ sheet (which is dominated by in-plane d_{xy} orbitals) even if the superconductivity is suppressed fully on α and β sheets. The effect of the SOC is also larger on α-β and so it is the combination of B-field and SOC that suppresses pairing on those sheets, while the external field has less of a direct effect on the γ sheet pairing. The fact that, as can be seen in Fig. 8(b), is it suppressed to a small residual pairing on α-β and not totally to zero could result from a "proximity" coupling between the superconducting γ sheet and the nonsuperconducting α-β ones as originally proposed by Zhitomirsky and Rice [45]. This can be seen in the lower three panels of Fig. 9, where we present the superconducting gap on three cylinders of the Fermi surface at the field value of 2.67 T (equal to the lower critical field H_{c1}). As expected, at this value of the field, the gap on α and β sheets is strongly suppressed leaving only the γ sheet superconducting. At higher field of $H_{c1} < 2.97T < H_{c2}$, presented in Fig. 10, the gap has almost completely vanished on the α and β sheets, remaining finite only on the γ sheet.

In contrast, the E_g state is more three-dimensional in nature and, as shown in the upper three panels of Fig. 9, it seems

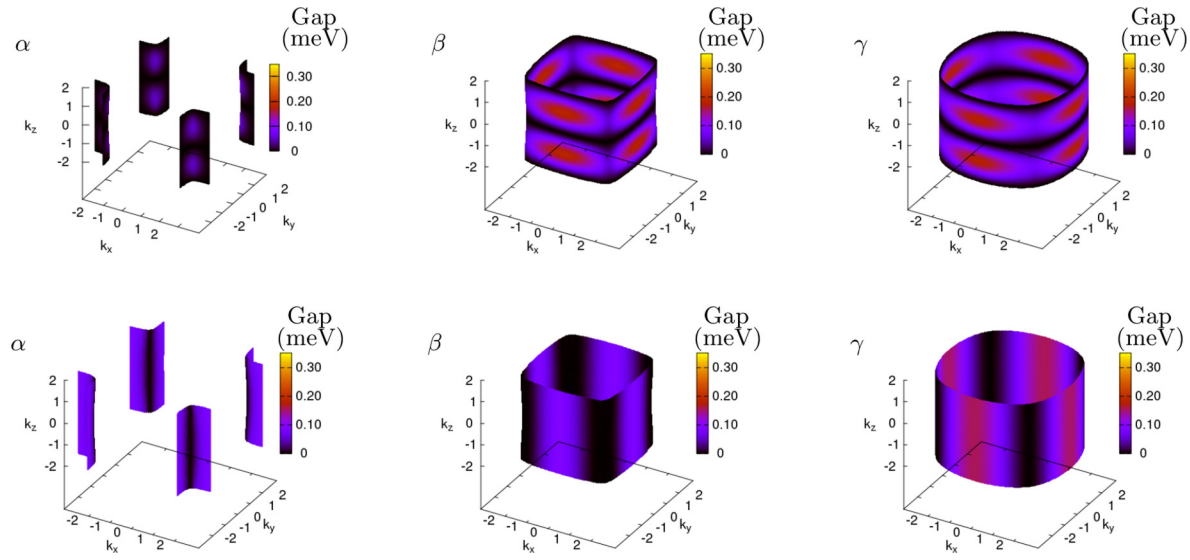

FIG. 9. Superconducting gap plotted at a field of 2.67 T on the normal-state Fermi surface. The upper row is for E_g pairing, while lower row is for B_{1g} pairing. Note that for the more two-dimensional nature of the B_{1g} pairing, the superconducting gap is significantly suppressed on the α and β sheets (of dominantly out-of-plane d_{xz} and d_{yz} character) as compared to the γ sheet (of dominantly in-plane d_{xy} character). In contrast, for the E_g pairing the gap size is comparable on all three Fermi sheets.

that the superconducting state, if it exists, must exist on all three sheets. Once it is destroyed on α-β, it can no longer be sustained independently on γ, and so superconductivity is suppressed simultaneously on all Fermi surface sheets. In this context, one can note that the quasiparticle gap remains roughly equal on all Fermi surface sheets for this pairing.

V. DISCUSSION

We have studied the d-wave pairing symmetries $d_{x^2-y^2}$ and $d_{xz} + id_{yz}$ within a realistic three-dimensional tight-binding model with the electron interaction treated via two off-site Hubbard U parameters, the latter fitted to reproduce the zero-field superconducting transition of 1.5 K. Reassuringly, the approach then captures with excellent quantitative agreement several other experimental findings: notably the specific-heat jump at zero field and the crossover temperature to Pauli limiting first-order transitions at finite field. For the Knight shift suppression (the ratio of superconducting to normal state susceptibilities) we find 80%, in good agreement with the most recent experimental data [8].

We find that $d_{x^2-y^2}$ and $d_{xz} + id_{yz}$ give very similar results for the Knight shift suppression, reduction in spin moment, and zero- and low-field heat capacities. However at large fields, in the strongly Pauli limiting region of the H-T phase diagram, these pairing symmetries reveal strikingly different behavior. For the chiral TRS breaking $d_{xz} + id_{yz}$ pairing, we find a single phase boundary of first-order transitions separating the normal and superconducting state. However, for $d_{x^2-y^2}$ pairing, the same region of the H-T phase diagram exhibits two phase boundaries: a line of first-order transitions extending from $T = 0$ and ending in a critical point at $T = 0.09$-0.22K exists in addition to the upper critical field line. On crossing this additional phase boundary, the material remains superconducting but suffers a significant reduction of the superconducting gap on the α and β Fermi sheets, with only a minimal change on the γ Fermi sheet. Variation of the Hubbard U parameters of our model (while ensuring that the zero-field critical temperature remains fixed at 1.5 K) reveals these findings to be qualitatively robust: for no parameters was an additional phase boundary line in the Pauli limiting regime found for $d_{xz} + id_{yz}$ pairing, while this feature was always present for $d_{x^2-y^2}$ pairing. However, the position

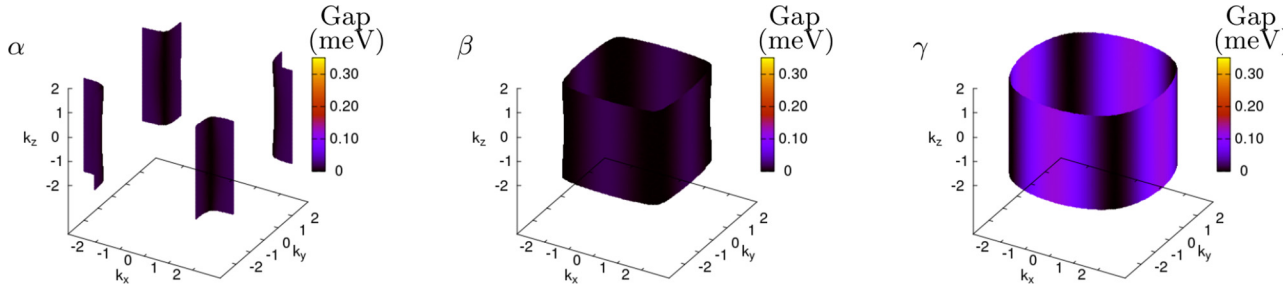

FIG. 10. Superconducting gap plotted at a field of 2.97 T on the normal-state Fermi surface for B_{1g} pairing. Whereas the superconducting gap has almost vanished on the α and β cylinders, the γ sheet remains superconducting.

of the phase boundary line is sensitive to the choice of U parameters.

In an earlier work exploring p-wave helical pairing [17], we found a high-field low-temperature structure of the phase diagram different from either of the pairing symmetries explored here, namely a lower critical field line that joined the bicritical point. Taken together this suggests that the Pauli limiting region of the H-T phase diagram may represent an interesting way to distinguish pairing symmetries in Sr_2RuO_4. A number of previous experimental works have described features at high fields that have some resemblance to those we report here, however it is fair to say that the high-field phase behavior is not conclusively established. The calculation we present here can be improved in the future by coupling the external field both with the spin (as we do here) and orbital (neglected in this work) degrees of freedom. This might be expected to bring our field values, generally too high by a factor $\sim$2, into better agreement with experiment. Nevertheless, as the novel physics of the H-T phase diagrams we report exist in the strongly Pauli limiting region of phase space (i.e., the contribution from the spin-coupling dominates), there is reason for optimism that they will be robust to the inclusion of orbital coupling of the field.

ACKNOWLEDGMENTS

This work was carried out using the computational facilities of the Advanced Computing Research Centre, University of Bristol. J.Q. and J.A. acknowledge support from EPSRC through the project "Unconventional Superconductors: New paradigms for new materials" (Grants No. EP/P00749X/1 and No. EP/P007392/1). M.G. thanks the visiting professorship program of the Centre for Dynamics and Topology at Johannes Gutenberg–University Mainz.

[1] T. M. Rice and M. Sigrist, Sr_2RuO_4: An electronic analogue of ^{3}He?, J. Phys.: Condens. Matter **7**, L643 (1995).

[2] K. D. Nelson, Z. Q. Mao, Y. Maeno, and Y. Liu, Odd-parity superconductivity in Sr_2RuO_4, Science **306**, 1151 (2004).

[3] M. Rice, Superfluid helium-3 has a metallic partner, Science **306**, 1142 (2004).

[4] K. Ishida, H. Mukuda, Y. Kitaoka, K. Asayama, Z. Q. Mao, Y. Mori, and Y. Maeno, Spin-triplet superconductivity in Sr_2RuO_4 identified by 17o knight shift, Nature (London) **396**, 658 (1998).

[5] K. Ishida, H. Mukuda, Y. Kitaoka, Z. Q. Mao, H. Fukazawa, and Y. Maeno, Ru NMR probe of spin susceptibility in the superconducting state of Sr_2RuO_4, Phys. Rev. B **63**, 060507(R) (2001).

[6] G. M. Luke, Y. Fudamoto, K. M. Kojima, M. I. Larkin, J. Merrin, B. Nachumi, Y. J. Uemura, Y. Maeno, Z. Q. Mao, Y. Mori, H. Nakamura, and M. Sigrist, Time-reversal symmetry-breaking superconductivity in Sr_2RuO_4, Nature (London) **394**, 558 (1998).

[7] J. Xia, Y. Maeno, P. T. Beyersdorf, M. M. Fejer, and A. Kapitulnik, High Resolution Polar Kerr Effect Measurements of Sr_2RuO_4: Evidence for Broken Time-Reversal Symmetry in the Superconducting State, Phys. Rev. Lett. **97**, 167002 (2006).

[8] A. Chronister, A. Pustogow, N. Kikugawa, D. A. Sokolov, F. Jerzembeck, C. W. Hicks, A. P. Mackenzie, E. D. Bauer, and S. E. Brown, Evidence for even parity unconventional superconductivity in Sr_2RuO_4, Proc. Natl. Acad. Sci. (USA) **118**, e2025313118 (2021).

[9] A. W. Lindquist and H.-Y. Kee, Distinct reduction of knight shift in superconducting state of Sr_2RuO_4 under uniaxial strain, Phys. Rev. Res. **2**, 032055(R) (2020).

[10] K. Ishida, M. Manago, K. Kinjo, and Y. Maeno, Reduction of the 17o knight shift in the superconducting state and the heat-up effect by nmr pulses on Sr_2RuO_4, J. Phys. Soc. Jpn. **89**, 034712 (2020).

[11] S. Ghosh, A. Shekhter, F. Jerzembeck, N. Kikugawa, D. A. Sokolov, M. Brando, A. P. Mackenzie, C. W. Hicks, and B. J. Ramshaw, Thermodynamic evidence for a two-component superconducting order parameter in Sr_2RuO_4, Nat. Phys. **17**, 199 (2021).

[12] S. Benhabib, C. Lupien, I. Paul, L. Berges, M. Dion, M. Nardone, A. Zitouni, Z. Q. Mao, Y. Maeno, A. Georges, L. Taillefer, and C. Proust, Ultrasound evidence for a two-component superconducting order parameter in Sr_2RuO_4, Nat. Phys. **17**, 194 (2021).

[13] V. Grinenko, S. Ghosh, R. Sarkar, J.-C. Orain, A. Nikitin, M. Elender, D. Das, Z. Guguchia, F. Brückner, M. E. Barber, J. Park, N. Kikugawa, D. A. Sokolov, J. S. Bobowski, T. Miyoshi, Y. Maeno, A. P. Mackenzie, H. Luetkens, C. W. Hicks, and H.-H. Klauss, Split superconducting and time-reversal symmetry-breaking transitions in Sr_2RuO_4 under stress, Nat. Phys. **17**, 748 (2021).

[14] S. Kashiwaya, K. Saitoh, H. Kashiwaya, M. Koyanagi, M. Sato, K. Yada, Y. Tanaka, and Y. Maeno, Time-reversal invariant superconductivity of Sr_2RuO_4 revealed by josephson effects, Phys. Rev. B **100**, 094530 (2019).

[15] W.-S. Wang, C.-C. Zhang, F.-C. Zhang, and Q.-H. Wang, Theory of Chiral p-Wave Superconductivity with Near Nodes for Sr_2RuO_4, Phys. Rev. Lett. **122**, 027002 (2019).

[16] A. T. Rømer, D. D. Scherer, I. M. Eremin, P. J. Hirschfeld, and B. M. Andersen, Knight Shift and Leading Superconducting Instability from Spin Fluctuations in Sr_2RuO_4, Phys. Rev. Lett. **123**, 247001 (2019).

[17] R. Gupta, T. Saunderson, S. Shallcross, M. Gradhand, J. Quintanilla, and J. Annett, Superconducting subphase and substantial knight shift in Sr_2RuO_4, Phys. Rev. B **102**, 235203 (2020).

[18] H. S. Røising, T. Scaffidi, F. Flicker, G. F. Lange, and S. H. Simon, Superconducting order of Sr_2RuO_4 from a three-dimensional microscopic model, Phys. Rev. Res. **1**, 033108 (2019).

[19] V. Grinenko, D. Das, R. Gupta, B. Zinkl, N. Kikugawa, Y. Maeno, C. W. Hicks, H.-H. Klauss, M. Sigrist, and R. Khasanov, Unsplit superconducting and time reversal symmetry breaking transitions in Sr_2RuO_4 under hydrostatic pressure and disorder, Nat. Commun. **12**, 3920 (2021).

[20] R. Sharma, S. D. Edkins, Z. Wang, A. Kostin, C. Sow, Y. Maeno, A. P. Mackenzie, J. C. S. Davis, and V. Madhavan, Momentum-resolved superconducting energy gaps of Sr_2RuO_4

from quasiparticle interference imaging, Proc. Natl. Acad. Sci. (USA) **117**, 5222 (2020).

[21] J. F. Annett, Symmetry of the order parameter for high-temperature superconductivity, Adv. Phys. **39**, 83 (1990).

[22] K. Deguchi, M. A. Tanatar, Z. Mao, T. Ishiguro, and Y. Maeno, Superconducting double transition and the upper critical field limit of Sr_2RuO_4 in parallel magnetic fields, J. Phys. Soc. Jpn. **71**, 2839 (2002).

[23] S. NishiZaki, Y. Maeno, and Z. Mao, Changes in the superconducting state of sr 2ruo 4 under magnetic fields probed by specific heat, J. Phys. Soc. Jpn. **69**, 572 (2000).

[24] Z. Q. Mao, Y. Maeno, S. NishiZaki, T. Akima, and T. Ishiguro, In-Plane Anisotropy of Upper Critical Field in Sr_2RuO_4, Phys. Rev. Lett. **84**, 991 (2000).

[25] S. Yonezawa, T. Kajikawa, and Y. Maeno, Specific-heat evidence of the first-order superconducting transition in Sr_2RuO_4, J. Phys. Soc. Jpn. **83**, 083706 (2014).

[26] S. Yonezawa, T. Kajikawa, and Y. Maeno, First-Order Superconducting Transition of Sr_2RuO_4, Phys. Rev. Lett. **110**, 077003 (2013).

[27] S. Kittaka, A. Kasahara, T. Sakakibara, D. Shibata, S. Yonezawa, Y. Maeno, K. Tenya, and K. Machida, Sharp magnetization jump at the first-order superconducting transition in Sr_2RuO_4, Phys. Rev. B **90**, 220502(R) (2014).

[28] N. Kikugawa, T. Terashima, S. Uji, K. Sugii, Y. Maeno, D. Graf, R. Baumbach, and J. Brooks, Superconducting subphase in the layered perovskite ruthenate Sr_2RuO_4 in a parallel magnetic field, Phys. Rev. B **93**, 184513 (2016).

[29] K. Kinjo, M. Manago, S. Kitagawa, Z. Q. Mao, S. Yonezawa, Y. Maeno, and K. Ishida, Superconducting spin smecticity evidencing the fulde-ferrell-larkin-ovchinnikov state in Sr_2RuO_4, Science **376**, 397 (2022).

[30] J. F. Annett, B. L. Györffy, G. Litak, and K. I. Wysokiński, Gap nodes and time reversal symmetry breaking in strontium ruthenate, Eur. Phys. J. B **36**, 301 (2003).

[31] M. Gradhand, K. I. Wysokinski, J. F. Annett, and B. L. Györffy, Kerr rotation in the unconventional superconductor Sr_2RuO_4, Phys. Rev. B **88**, 094504 (2013).

[32] J. Robbins, J. F. Annett, and M. Gradhand, Effect of spin-orbit coupling on the polar kerr effect in Sr_2RuO_4, Phys. Rev. B **96**, 144503 (2017).

[33] A. Tamai, M. Zingl, E. Rozbicki, E. Cappelli, S. Riccò, A. de la Torre, S. McKeown Walker, F. Y. Bruno, P. D. C. King, W. Meevasana, M. Shi, M. Radović, N. C. Plumb, A. S. Gibbs, A. P. Mackenzie, C. Berthod, H. U. R. Strand, M. Kim, A. Georges, and F. Baumberger, High-Resolution Photoemission on Sr_2RuO_4 Reveals Correlation-Enhanced Effective Spin-Orbit Coupling and Dominantly Local Self-Energies, Phys. Rev. X **9**, 021048 (2019).

[34] M. Braden, P. Steffens, Y. Sidis, J. Kulda, P. Bourges, S. Hayden, N. Kikugawa, and Y. Maeno, Anisotropy of the Incommensurate Fluctuations in Sr_2RuO_4: A Study with Polarized Neutrons, Phys. Rev. Lett. **92**, 097402 (2004).

[35] C. Bergemann, S. R. Julian, A. P. Mackenzie, S. NishiZaki, and Y. Maeno, Detailed Topography of the Fermi Surface of Sr_2RuO_4, Phys. Rev. Lett. **84**, 2662 (2000).

[36] K. Iida, M. Kofu, K. Suzuki, N. Murai, S. Ohira-Kawamura, R. Kajimoto, Y. Inamura, M. Ishikado, S. Hasegawa, T. Masuda, Y. Yoshida, K. Kakurai, K. Machida, and S. Lee, Horizontal line nodes in Sr_2RuO_4 proved by spin resonance, J. Phys. Soc. Jpn. **89**, 053702 (2020).

[37] I. A. Firmo, S. Lederer, C. Lupien, A. P. Mackenzie, J. C. Davis, and S. A. Kivelson, Evidence from tunneling spectroscopy for a quasi-one-dimensional origin of superconductivity in sr_2ruo_4, Phys. Rev. B **88**, 134521 (2013).

[38] H. Suderow, V. Crespo, I. Guillamon, S. Vieira, F. Servant, P. Lejay, J. P. Brison, and J. Flouquet, A nodeless superconducting gap in $Sr_2RuO_4$from tunneling spectroscopy, New J. Phys. **11**, 093004 (2009).

[39] S. Kittaka, S. Nakamura, T. Sakakibara, N. Kikugawa, T. Terashima, S. Uji, D. A. Sokolov, A. P. Mackenzie, K. Irie, Y. Tsutsumi, K. Suzuki, and K. Machida, Searching for gap zeros in Sr_2RuO_4 via field-angle-dependent specific-heat measurement, J. Phys. Soc. Jpn. **87**, 093703 (2018).

[40] A. P. Mackenzie, S. R. Julian, A. J. Diver, G. J. McMullan, M. P. Ray, G. G. Lonzarich, Y. Maeno, S. Nishizaki, and T. Fujita, Quantum Oscillations in the Layered Perovskite Superconductor Sr_2RuO_4, Phys. Rev. Lett. **76**, 3786 (1996).

[41] A. J. Leggett, A theoretical description of the new phases of liquid ^{3}He, Rev. Mod. Phys. **47**, 331 (1975).

[42] A. N. Petsch, M. Zhu, M. Enderle, Z. Q. Mao, Y. Maeno, I. I. Mazin, and S. M. Hayden, Reduction of the Spin Susceptibility in the Superconducting State of Sr_2RuO_4 Observed by Polarized Neutron Scattering, Phys. Rev. Lett. **125**, 217004 (2020).

[43] J. Robbins, J. F. Annett, and M. Gradhand, Theory of the orbital moment in a superconductor, Phys. Rev. B **101**, 134505 (2020).

[44] A. Petsch (private communication).

[45] M. E. Zhitomirsky and T. M. Rice, Interband Proximity Effect and Nodes of Superconducting Gap in Sr_2RuO_4, Phys. Rev. Lett. **87**, 057001 (2001).